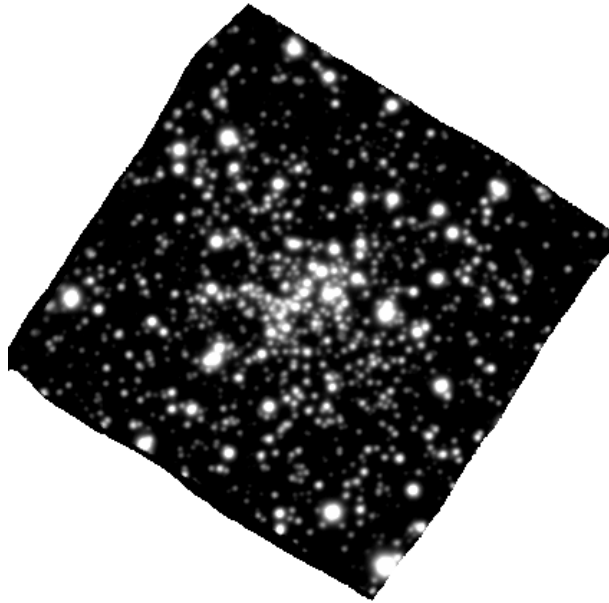




---

# Spectroscopic and photometric analysis of NGC6397

---



MINOR THESIS

submitted in partial fulfillment of the  
requirements for the degree of

MASTER OF SCIENCE  
in  
ASTRONOMY

|                             |                         |
|-----------------------------|-------------------------|
| Author :                    | Alexander G. M. Pietrow |
| Student ID :                | 1054678                 |
| Supervisor :                | Dr. Jarle Brinchmann    |
| 2 <sup>nd</sup> corrector : | Dr. Jan Lub             |

Leiden, The Netherlands, July 31, 2015



# Spectroscopic and photometric analysis of NGC6397

**Alexander G. M. Pietrow**

Leiden Observatory , Leiden University  
P.O. Box 9500, 2300 RA Leiden, The Netherlands

November 17, 2015

## **Abstract**

Using the MUSE instrument we were able to get both photometric and spectral data from the globular cluster NGC 6397. From these data we were able to infer the age and mass of this cluster while setting a metallicity and IMF. We did this by creating integrated spectra of the cluster over large areas up to 30'' in radius. These quantities were compared to literature and data obtained from photometry of resolved stars. By doing this we want to see how accurately we can obtain these values from unresolved galaxies at large distances and have developed a method that gives consistent results for regions larger than 10'' in radius. For the largest region tested we found a mass of  $640.7 \pm 170 M_{\odot}$  and  $463.79 \pm 170 M_{\odot}$  for the Salpeter and Chabrier IMFs respectively. Both off by more than 10% with the literature value of 580.87 but within the margin of error. Due to the large errors, the differences in mass were not statistically significant and no distinction can be made between the two IMFs. The logarithm of the age fitted the literature value but also had large errorbars. The found  $\log(\text{age})$  was  $9.96 \pm 0.38$  and  $9.93 \pm 0.37$  when using the Chabrier and Salpeter IMFs respectively, while literature provided a value of  $10.11^{+0.01}_{-0.03}$ . This made us conclude that while some indicative quantities can be derived using this method, it should be studied further and that results obtained in this way should be regarded carefully.



# Contents

|          |                               |           |
|----------|-------------------------------|-----------|
| <b>1</b> | <b>Introduction</b>           | <b>1</b>  |
| <b>2</b> | <b>Method</b>                 | <b>7</b>  |
| 2.1      | Data                          | 7         |
| 2.2      | Data analysis                 | 8         |
| 2.2.1    | Regions                       | 8         |
| 2.2.2    | Photometry                    | 16        |
| 2.2.3    | Integrated Spectra            | 18        |
| <b>3</b> | <b>Results and Discussion</b> | <b>25</b> |
| 3.1      | Photometry                    | 25        |
| 3.1.1    | Convolution                   | 25        |
| 3.1.2    | Comparing MUSE to Hubble      | 25        |
| 3.1.3    | Integrated Spectra            | 26        |
| <b>4</b> | <b>Conclusion</b>             | <b>35</b> |
|          | References                    | 37        |



# Chapter 1

## Introduction

In 1764 Charles Messier looked at M4. To the naked eye it looked like a faint fuzzy cloud in the sky, but through a telescope he could see a great many stars. Messier had discovered the first globular cluster (GC). This discovery changed our view on the size of the universe, as previous discoveries (e.g. The Copernican solar system) had done many times before. Over the years Messier and other astronomers after him found many more globular clusters and other angularly compact celestial objects such as galaxies. All of these discoveries were made possible by the ever improving astronomical instruments.

The biggest problem with most of the aforementioned objects is that they are too far away to spatially resolve all of the individual sub-objects. GCs are the exception, which is why they play a crucial role in understanding stellar populations. They are close enough that their constituent stars can be resolved individually, and at the same time they are compact enough to test the methods we use on less resolvable targets. In this research project we will do just that and compare two methods of obtaining stellar parameters from one of the closest GCs, NGC 6397. These will be photometric observations of individual stars and spectroscopic integrations of specially large regions, containing dozens of stars.

Globular clusters are not only interesting because of their size and resolvability, but also because common belief suggests that all the stars in these clusters are formed at roughly the same time. This simple fact caused them to become a favourite research subject of many astronomers over the last 60 years, as it makes them a goldmine for the field of stellar evolution and categorization. Populations like these can be approximated by a simple stellar population (SSP) (Puzia et al., 2002), which are well described

in Conroy (2013). For this reason we will summarize the relevant information from Conroy (2013) to give an outline of the theory behind SSP's. Here we assume that all stars have the same age, metallicity and abundance pattern. They can therefore be described by a set of isochrones, a proper set of stellar spectral libraries and initial mass function (IMF), as can be seen in Fig. 1.1.

Isochrones describe specific tracks on the Hertzsprung-Russel diagram (HRD) for stars with identical age and metallicity, but different masses. Ideally they sample everything between the minimum and maximum possible stellar mass, which ranges from roughly  $0.1 M_{\odot}$  to  $100 M_{\odot}$ . However, due to the fact that we can only see a finite amount of stars, we currently only have discrete samples of these lines. Especially near fast evolutionary phases this can cause a large error which has to be corrected. Designers of isochrones pay special attention to this fact and minimize these effects (e.g. Charlot and Bruzual (1991)). A key weakness of all of these models is that they are one dimensional, requiring estimations for three dimensional processes like convection, rotation, mass loss, close binary interaction and stellar remnants. Corrections for these effects are often empirically obtained and added to the isochrones to match them with observations as a form of calibration. For this research project we use the Padova 94 evolutionary track (Bertelli et al., 1994; Girardi et al., 2000), the most widely used isochrone table, which works well for most age and metallicity ranges, but falls short for young ages. However we know that NGC 6397 is relatively old ( $12.8^{+0.50}_{-0.75}$  Gyr e.g. Torres et al. (2015)), so this shortcoming does not matter.

Stellar spectral libraries convert outputs of stellar evolution calculations (e.g. luminosity, surface gravity ( $\log(g)$ ) and effective temperatures as a function of metallicity) into observable spectral energy distributions (SEDs). The problem here is that we do not have a single library neither, empirical or theoretical that described the entire parameter space needed for constructing SSP models. Therefore we often need to combine several libraries of varying qualities, significantly raising the uncertainty of fitted SSPs. The major disadvantage with theoretical libraries is that they depend heavily on the input parameters, while for empirical libraries we can only look at local stars to get high accuracy. This means that we cannot assume that these stars are representative for the entire range of possible stars. The software that we use for this project uses the empirical STELIB (Le Borgne et al., 2003) spectral library in the range between 3200 and 9500 Å, and the theoretical, empirically recalibrated BaSeL 3.1 (Westera et al., 2002) spectral library outside that range (Bruzual and Charlot, 2003c). However, since our data, ranging from 4650 to 9300 Å, falls com-

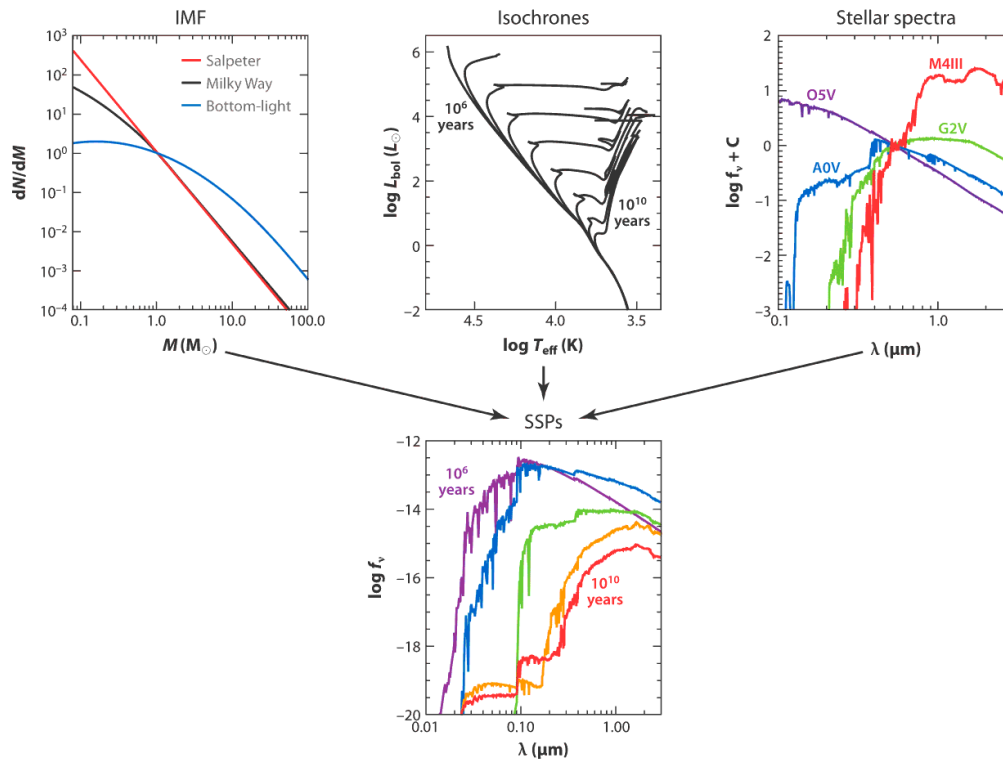


**Figure 1.1:** An overview of the stellar population synthesis (SPS) method. The three upper panels show the ingredients needed for an SSP. An IMF, isochrones for a given age and metallicity range, and stellar spectra for a given effective temperatures, luminosities and metallicities are combined into a SSP model. Varying any of the input parameters can strongly influence the outcome. Figure from (Conroy, 2013).

pletely within the STELIB range, we will only be using that.

IMFs give the initial mass distribution of a stellar population. These functions often are interpreted as a probability density function (PDF) for the initial mass of every single star. They determine the overall normalization of the mass to light ratios and the rate of luminosity evolution of a stellar population. IMFs have been a subject of study for decades and because of that there are many IMFs around. The most popular IFMs are Salpeter (Salpeter, 1955), Scalo (Miller and Scalo, 1979), Kroupa (Kroupa, 2001) and Chabrier (Chabrier, 2003). Given the fact that there are so many, it is important to look at different IFMs. For this reason both the Salpeter and Chabrier IMFs have been used for this project.

SSP models are usually taken as a given, and then fitted to observational data, from which we can infer metallicity and other parameters. As

mentioned before, we can test these models against more conventional photometric methods, such as CMDs, by looking at GCs. Using these we can compare the age, mass, metallicity and other parameters derived via photometric analysis of a resolved population to the same parameters obtained via spectral modelling of an identical but unresolved population. Assuming that the methods for resolved populations are correct, we can calibrate our methods for unresolved populations to give similar results, thus making tools for studying the universe at distances where galaxies cannot be resolved into individual stars. Besides broadband photometry, there are two main ways of inferring physical properties of compact objects: long-slit spectroscopy (LSS) and integral field spectroscopy (IFS).

When using a Long-slit spectrograph, we make use of a slit which is spatially larger in one axis than the object that we wish to observe. In our case the core of a spatially extended GC. This slit is pointed slightly off target, usually one core radius, and is then allowed to drift across the cluster with a certain trail rate. In this way we obtain one integrated spectrum of the entire object and all its parts. Additionally we need a suitable background. When the source is small enough, this can be taken from the outer edges of the slit. If the source is too extended, or other sources contaminate the edges, a separate background is needed. This can be obtained from a selected patch of empty sky that matches the objects background. Especially near the Galactic bulge this is important as the background does not have a uniform extinction (Schiavon et al., 2005).

IFS is a relatively new method where the spectra of several nearby areas are taken in order to make a 'spectroscopic image' that consists of an array of spatial pixels (spaxels), where every spaxel contains a spectrum. So a single spaxel can be seen as a spectrum, while spatial information can be gained from tiling spaxels. So a normal spectrometer is an 1x1 integral field unit (IFU). Such a cube can be cut at any  $\lambda$  to see how that piece of sky would look in that wavelength. Allowing us to simulate any filter by setting the weight on every wavelength layer. In this way photometry and spectroscopy can be combined when using IFU data. Currently, the leading IFU is the Very Large Telescopes (VLT) Multi Unit Spectroscopic Explorer (MUSE). MUSE has a field of view of 1x1 arcmin<sup>2</sup> and is sampled by 0.2x0.2 arcsec<sup>2</sup> spaxels. Its simultaneous spectral range is 0.465 - 0.93  $\mu$ m and it has a resolution of  $R \sim 3000$  (Bacon et al., 2006). Where  $R$  is the resolving power of the instrument, given by  $R = \lambda / \Delta\lambda$ . Here  $\Delta\lambda$  is the smallest difference in wavelength that can be distinguished at a wavelength  $\lambda$ . For the first time, this instrument allows us to get spectra of every individual star in a cluster while keeping the photometric details.

In this research project we will look at the photometry of NGC 6397, as well as its integrated spectrum. This close by, 2.2 Kpc (Harris, 1996), metal poor,  $\text{Fe}/\text{H} = -1.76$  (Forbes and Bridges, 2010), core collapsed cluster has been the subject of many detailed photometric and spectroscopic studies (Alcaino et al., 1997; Shara, 2000; Heyl et al., 2012), and is a perfect candidate for testing our methods. With recent MUSE observations we will be able to test the 'truth' locally by comparing parameters obtained from counting stars and our own 'integrated' spectra, which are made by spatially adding spaxels into one larger spaxel. Besides that we will also use data from the MUSE group of the Goettingen Institut for Astrophysik, provided by dr. Sebastian Kamann.

First we will look into the kind of data that we are using and the methods for extracting information from this data in the 'Methods' section. Next we will look at the results obtained from applying these methods and discuss their meaning in the 'Results and Discussion' section and finally we will end with concluding remarks in the 'conclusion'.



# Method

## 2.1 Data

The NGC6397 MUSE datacube was obtained at Paranal Observatory, during the third MUSE commissioning run, using the MUSE instrument mounted on UT4 (Yepun) of the Very large Telescope (VLT). The data was taken on the 27th of August 2014 with an exposure time of 60s for all four pointings, a maximum seeing of 2'' and brightness units of  $10^{-20}$  erg/s/cm<sup>2</sup>/Å. This is the central cube from a 5x5 mosaic of the entire GC centered at RA = 265.16617, Dec = -53.670943. Each pointing was observed with a dither pattern of about 1' and after offsetting the derotator by 90 degrees to ensure that each star falls onto multiple spectrographs, ensuring a homogeneous image quality. The data reduction pipeline by Weilbacher et al. (2014) takes care of the bias, flat field and wavelength calibrations and combines the individual frames into a single cube (Husser et al., 2015). The cube ranges from 4650 to 9300 Å in the wavelength direction.

For the photometric counterparts of the cube we used three Hubble Space Telescope (HST) images of the same cluster, which were observed in the F435W, F606W, F814W filters. All three images are obtained from the `mast.stsci.edu` website with brightness units of electron/sec and are chosen for their low level of bleeding stars. We do this because bleeding stars lose counts when oversaturated and change the spatial location of the light, making comparisons harder. An overview of the images can be seen in Table 2.1.

The filter transmission curves for the three HST images are taken from <http://svo2.cab.inta-csic.es>. All three are from the ACS\_WFC camera where we used the -81 C<sup>0</sup> transmission curves as all observations are from after 2006 (Mack et al., 2007). (The HST lowered its CCD temperature from

| Filter | Ra           | Dec         | $T_{exp}$ | date       |
|--------|--------------|-------------|-----------|------------|
| F435w  | 265.16527    | -53.671744  | 353 s     | 28-06-2008 |
| F606w  | 265.17227505 | -53.6741057 | 61 s      | 31-01-2008 |
| F814w  | 265.17227505 | -53.6741057 | 61 s      | 31-01-2008 |

**Table 2.1:** Three HST images in different filters. Chosen for their short enough exposure time, minimizing the amount and severity of bleeding stars.

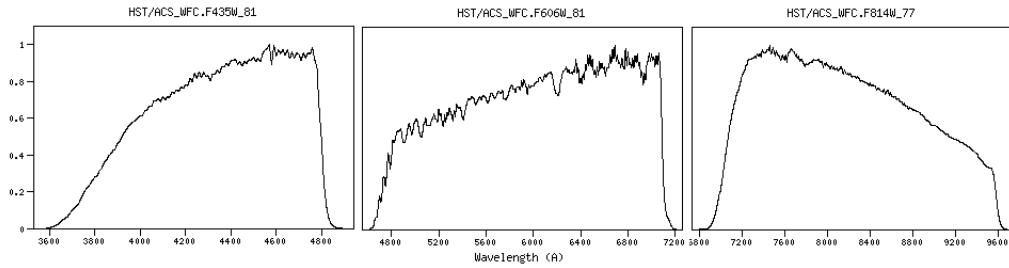


**Figure 2.1:** The three filters used. *f435w*, *f606w* and *f814w*.

-77 to -81  $C^0$  in 2006.)

Individual stellar parameters were derived by Dr. Sebastian Kamann and Dr. Tim-Oliver Husser from the Goettingen Institut for Astrophysik and shared through personal correspondence. This data will be referred to as the data by dr. Kamann.

## 2.2 Data analysis

### 2.2.1 Regions

For both the spectral and the photometric analysis, we used a set of 28 concentric circles, shown in Fig. 2.2. These circles, not annuli, are centred around the middle of the image (RA = 17:40:41.695, DEC = -53:40:27.52,3) to allow for the largest one to cover the most area. The circles range from 2 to 30 arcseconds with increments of 1". The core center is not far from this point, at RA = 17:40:42.09, DEC=-53:40:27.6 (Martinazzi et al., 2014). Besides that there is a separate background region (circle 29) as alternative to the automatic background subtraction routines, since these do not function well in a crowded area (See Fig. 2.3). We chose these regions because of their good sampling of the central core center and steady increase in mass. We did not look at other non overlapping areas because of the large CPU time which is required for every region. To get a basic under-

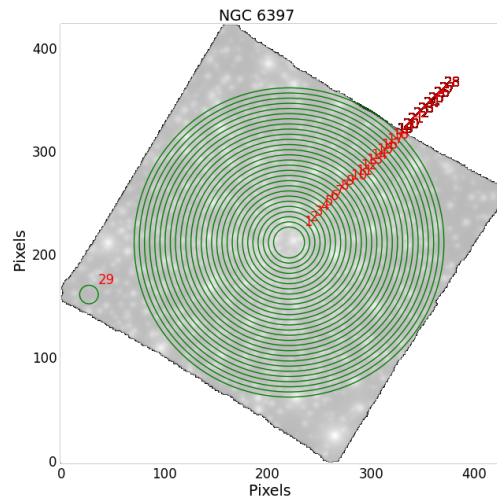


**Figure 2.2:** A white light image with 28 concentric regions and one background marked as the 29th circle. The largest ring almost samples the entire cube.

standing of these regions we did a series of tests to learn more about the distribution of stars in the regions. In these tests we will look at the mass, temperature and metallicity of the cluster to see how these quantities vary as a function of radius and if these variations become constant at some radius. To see this we will look at the stars as both a function of circle radius and the individual stars themselves.

We start by looking at the mass distribution of the cluster. In Fig. 2.4a we can see a plot of the clusters largest circle. Instead of color coding every individual star, we chose to interpolate between them to create a more easy to view image. From this image we can immediately see that the mass fluctuates the strongest in the center and the lower left quadrant. However, if we sum the mass from every circle, we will see that once the radius is large enough, e.g. 10", the fluctuations average out and the mass increases linearly. (Fig. 2.4b) This will make it easier to compare the different circles with each other. In Fig. 2.4c we can see the distribution of the mass of the individual stars. We see that this peaks around  $0.7 M_{\odot}$ .

When looking at the temperature in Fig. 2.5a we can see an interpolated plot with individual temperatures, similar to the mass plot above. This plot shows the individual temperatures of the separate stars. Apart from a few hot and cold regions, this area is relatively homogeneous, this is confirmed by Fig. 2.5c, where we have plotted a histogram of the temperatures. Here we can see that most stars are around 6000 K with a few

exceptions. The hot stars in the center will cause the average temperature per circle to start out jumpy, but eventually this will even out to a certain temperature. This average is calculated by taking the sum of the temperature times the luminosity of every star. This number is then divided by the sum of the luminosity. (See Eq. 2.1) While this method is not exactly physically accurate, it prevents small hot stars from dominating the distribution and gives weight to cool giants. This allows us to get an idea about the distribution of stellar types throughout the cluster. These values are not used elsewhere and serve purely as a diagnostic tool.

$$\langle T_{\text{eff}} \rangle = \frac{\sum (T_{\text{eff}})_i \cdot L_{Vi}}{\sum L_{Vi}} \quad (2.1)$$

With  $\langle T_{\text{eff}} \rangle$  the average temperature,  $(T_{\text{eff}})_i$  the individual temperatures of every star and the individual luminosities,  $L_V = \frac{4\pi GM\sigma T^4}{g}$ . Here we replaced the radius with  $G$ , the gravitational constant, the mass  $M$  and  $g$ , the surface gravity using the following relation;  $R^2 = \sqrt{GM/g}$ .

In Fig. 2.5b we can see the result of this plot. There is a big peak at 5'' from the center, but from about 15'' from the center the 'temperature' stabilizes around 6050 K. Due to the non-physical nature of this temperature we can only use this method to look if it stabilises or not. If needed, the value should be derived properly.

Finally the metallicities are provided in terms of  $[\text{Fe}/\text{H}]$ , which is almost identical to the  $[\text{M}/\text{H}]$  fraction, allowing us to equate them. (Here  $[\text{Fe}/\text{H}]$  gives the iron abundance of the star compared to the Solar abundance and  $[\text{M}/\text{H}]$  the total abundance compared to that of our Sun.)

$$\left[ \frac{\text{Fe}}{\text{H}} \right] \approx \left[ \frac{\text{M}}{\text{H}} \right] = \log 10 \left( \frac{Z/X}{Z_{\odot}/X_{\odot}} \right). \quad (2.2)$$

Now if we imagine a GC with  $N$  stars, each having a metallicity  $\left(\frac{M}{H}\right)_i$ , we cannot simply average the metallicities to get the value that we would have obtained when looking at the same cluster while not resolving it. We need to sum the  $Z$  and  $X$  values inside of the equation to get a good average. However this means that we first need to get back the original fraction values.

We start by noting that  $X + Y + Z = 1$ . Where  $X$  is the hydrogen fraction,  $Y$  the helium fraction and  $Z$  all other elements above that. We have  $X$  and  $Z$ , but we can't solve this equation without  $Y$ . However because these are low metallicity stars, we can take  $Y$  to be the cosmological abundance as given by the Planck mission, and thus use  $Y_p$  for our  $Y$  value.  $\left(\frac{He}{H} = \frac{Y}{X} =$

0.085 (Aver et al. 2013; Payne 1925)). Solving the equation for  $Z$  and  $X$  then becomes a quick algebraic exercise, giving us the following relations.

$$Z = \frac{10^{M/H} \beta_{\odot}}{1 + 10^{M/H} \beta_{\odot}} \alpha \quad (2.3)$$

$$X = \frac{1}{10^{M/H} \beta_{\odot} + \alpha}. \quad (2.4)$$

With  $\alpha = 0.085$  and  $\beta_{\odot} = \frac{Z_{\odot}}{X_{\odot}} = 0.027$ . These values can be calculated for every star and multiplied by their mass, giving us the mass weighed metallicity

$$\begin{aligned} \left[ \frac{M}{H} \right] &= \log 10 \left( \beta_{\odot}^{-1} \frac{\frac{1}{M_{tot}} \sum_{i=0}^N Z_i \cdot M_i}{\frac{1}{M_{tot}} \sum_{i=0}^N X_i \cdot M_i} \right) \\ &= \log 10 \left( \beta_{\odot}^{-1} \sum_{i=0}^N \frac{Z_i \cdot M_i}{X_i \cdot M_i} \right). \end{aligned} \quad (2.5)$$

The results can be seen in Fig. 2.6. This again is built up out of an interpolated plot of the individual stars, showing little fluctuation in the center and some more near the outer edges. In Fig. 2.6c we see that once again after roughly the fifth circle the average metallicity stabilises into a linearly increasing relation. The histogram shows us that most stars have a metallicity between -2 and -3 with very few exceptions.

Taking these three tests into account, we can conclude that these regions should give reliable measurements from the 10th circle onwards. After the 15th any measurements should give roughly the same parameters for all the larger circles. This means that depending on the amount of data points that we want and the S/N that we are willing to settle with, we should use a minimal region of anything between 10 and 15'' in radius.

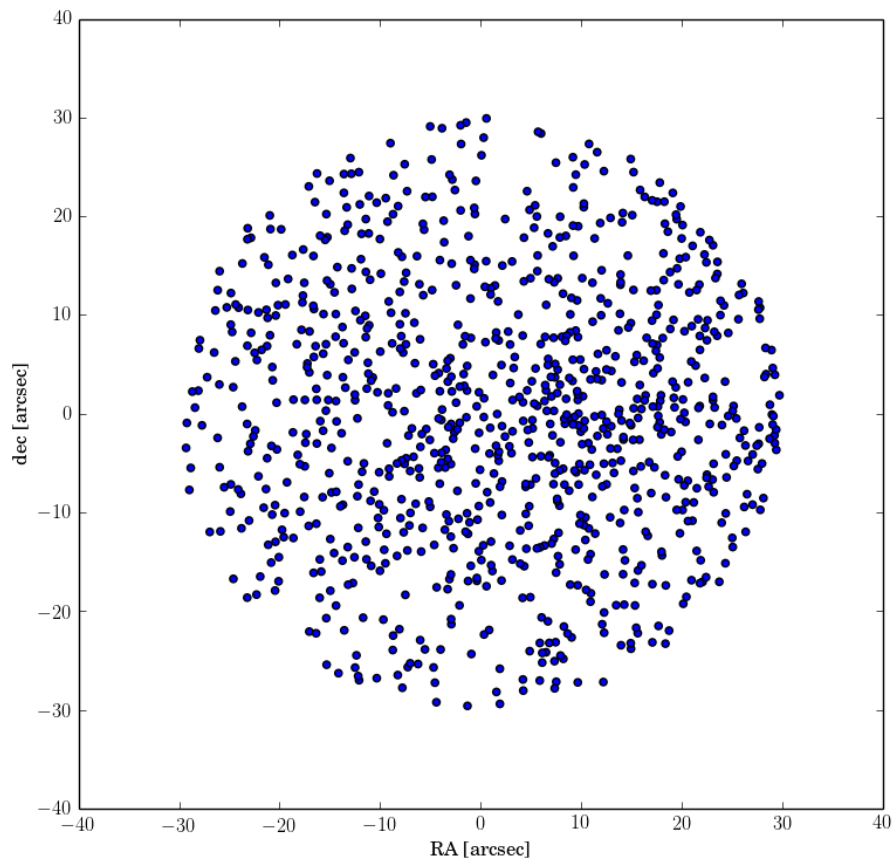


**Figure 2.3:** A plot showing the positions of all the stars contained in largest region, shown with equally large markers to see the overall distribution. The image is centred on  $RA = 265.16617$ ,  $Dec = -53.670943$ .

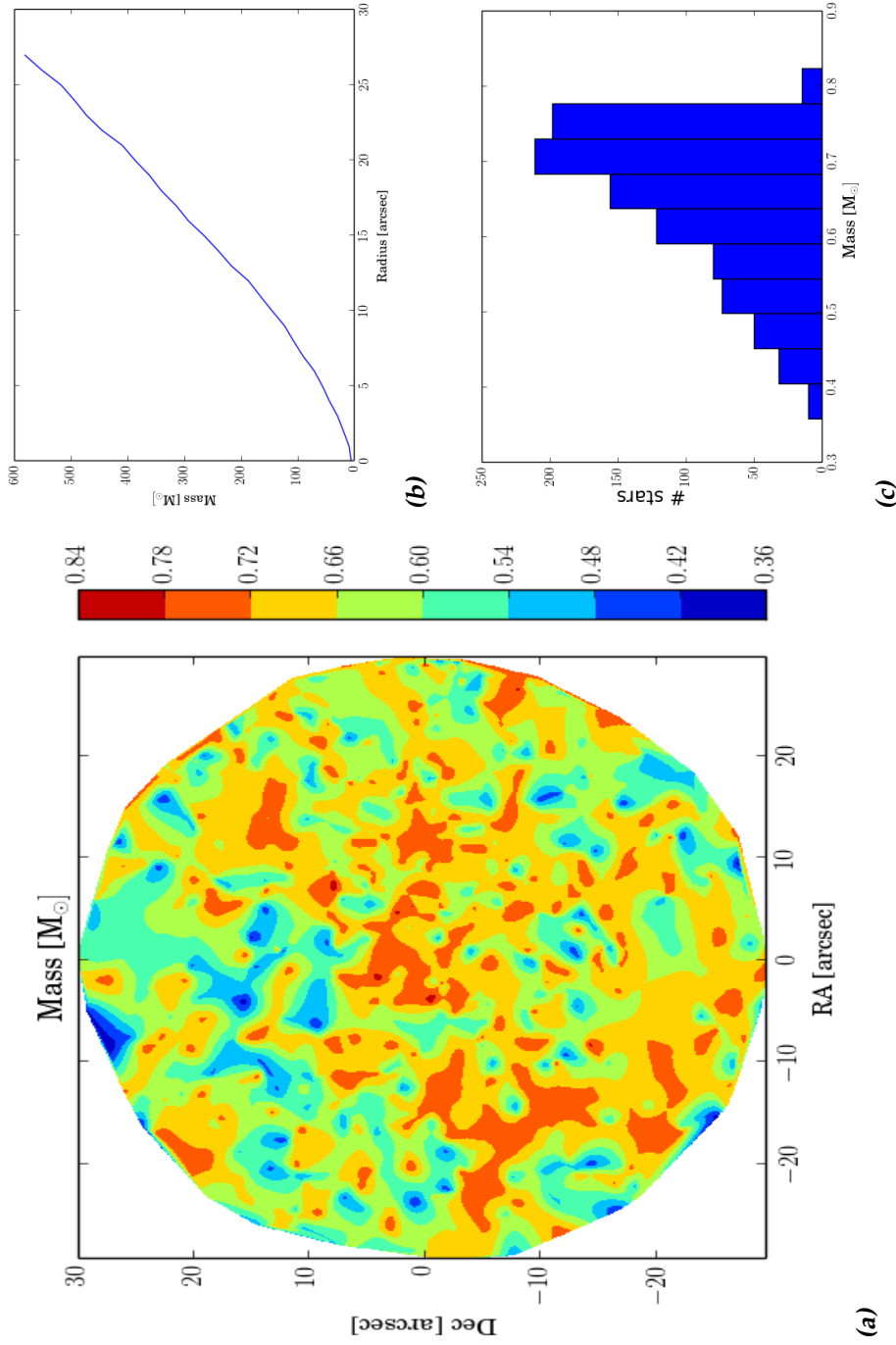


**Figure 2.4:** (a) A contour plot of the mass inside of the largest circle. It is an interpolation of the mass of the stars from Fig. 2.3, color coded with their mass. This was done to give a less cluttered image of the mass distribution. (b) A plot showing the sum of the mass inside of the circles as a function of radius of the circles. After about 10'' the mass increase becomes linear. (c) A histogram showing the distribution of masses of individual stars for the largest region.

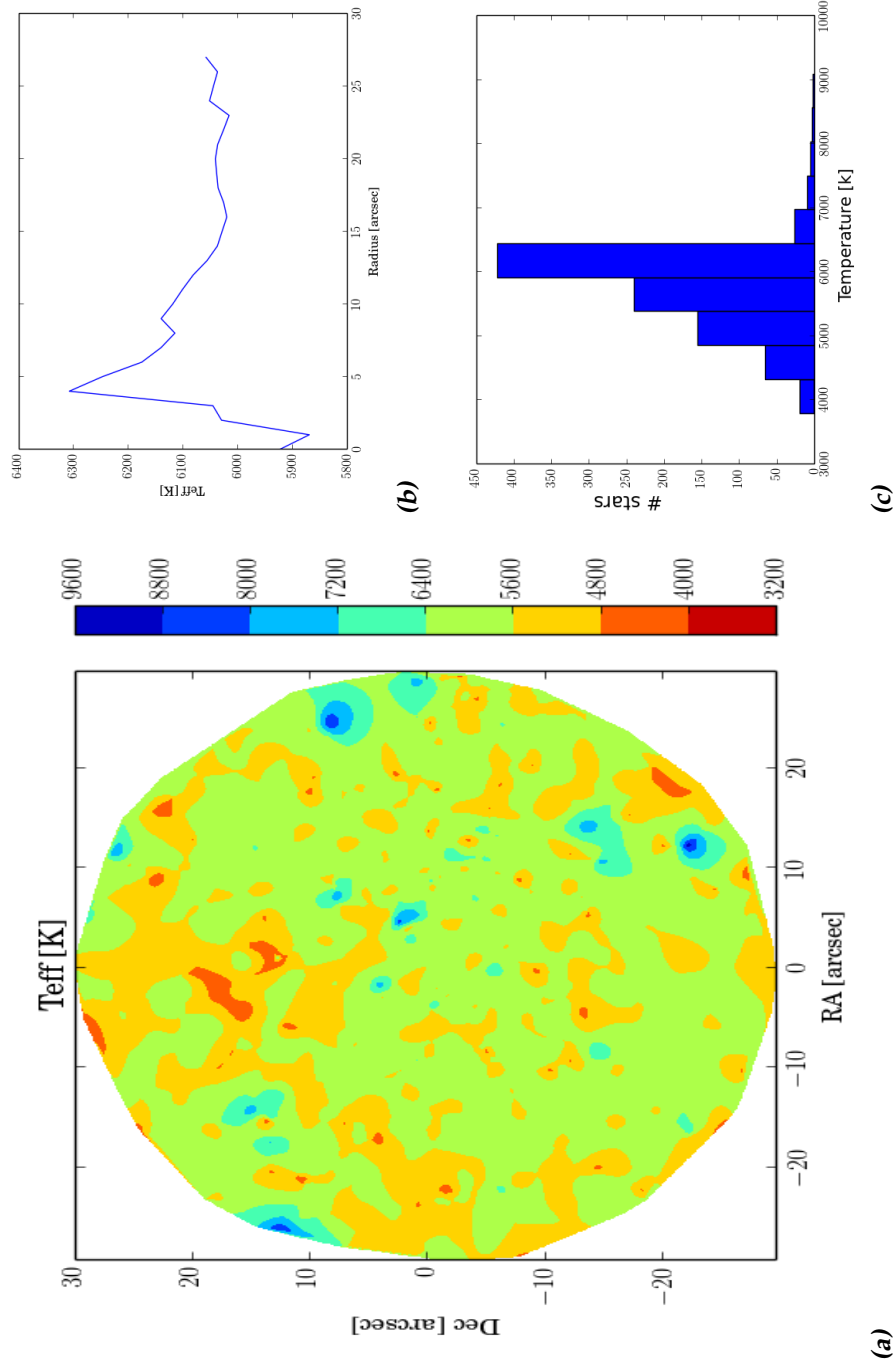


**Figure 2.5:** (a) A contour plot of the effective temperature inside of the largest circle. It is an interpolation of the the stars from Fig. 2.3, color coded with their temperature. This was done to give a less cluttered image of the mass distribution. (b) A plot showing the increase of mean temperature inside of the circles as a function of circle radius. At a radius of about  $10''$ , it starts to settle around a single value. (c) A histogram showing the distribution of temperatures of individual stars for the largest circle. The majority of the population is around 6000 K.

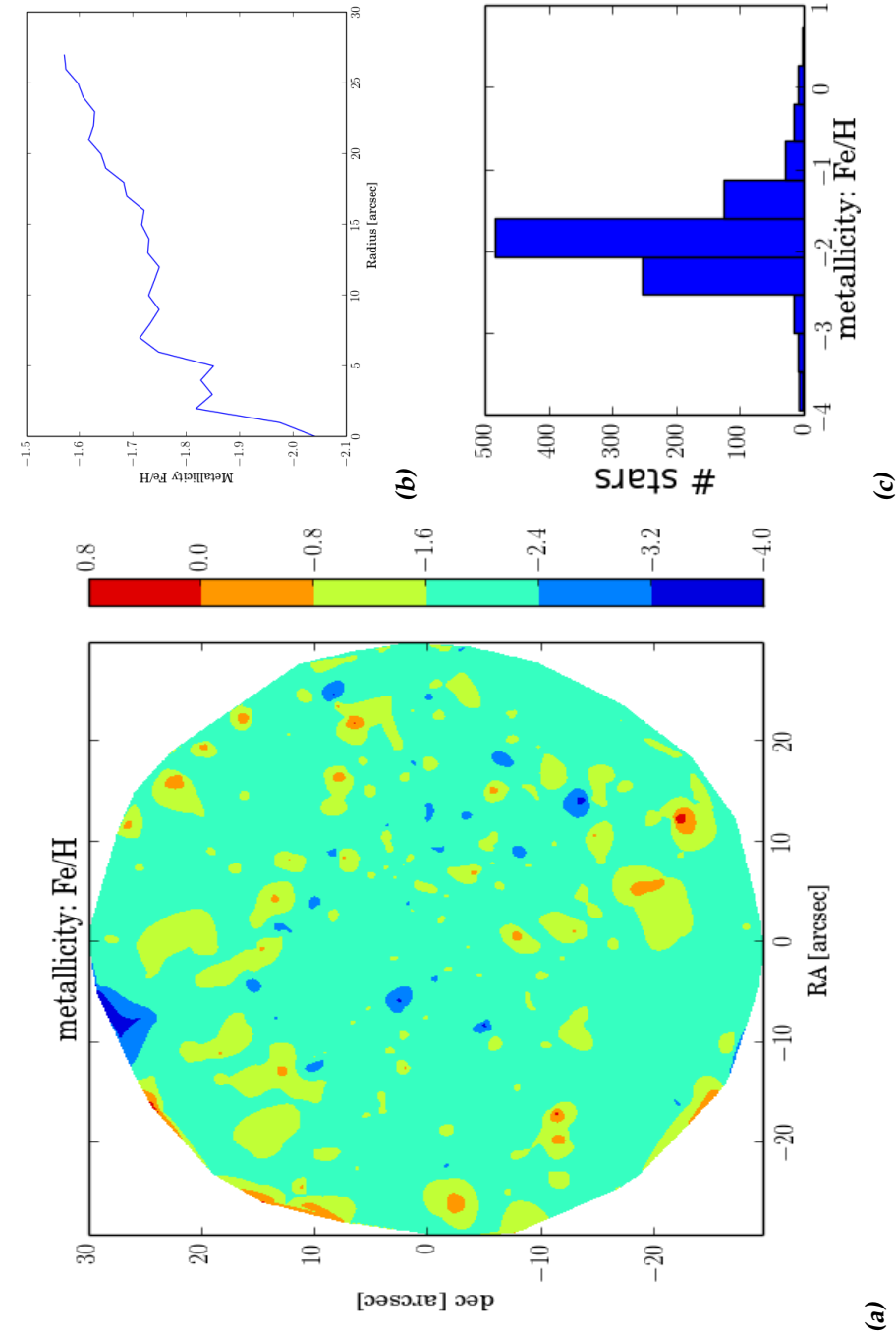


**Figure 2.6:** (a) A contour plot of the metallicity inside of the largest circle. It is an interpolation of the stars from Fig. 2.3, color coded with their metallicity. This was done to give a less cluttered image of the mass distribution. (b) A plot showing the increase of the average metallicity as described in Eq. ?? as a function of radius. After about 10'' we can see that the relation becomes roughly linear. (c) A histogram showing the distribution of metallicity of individual stars, relative to solar metallicity, for the largest circle.

## 2.2.2 Photometry

### Comparing MUSE to Hubble

The MUSE data cube can be summed up over the wavelength direction to obtain a white light image. If this axis is convolved with a HST transmission curve ( $R$ ) then we can mimic a Hubble picture and compare magnitudes.

$$F_{HST} = \int d\lambda F_{MUSE}(\lambda) R(\lambda) \quad (2.6)$$

For comparing the magnitudes we will use the ABmag system to get apparent magnitudes ( $m_{AB}$ ) that are calibrated on a hypothetical calibration source ( $C_\nu$ ). This source has a constant flux density of 3631 Jy for all frequencies  $\nu$ . (Oke and Gunn (1983), Fukugita et al. (1996)) The exact method for doing this can be found in Eq. 8 of Bruzual and Charlot (2003b), which is displayed below. This equation integrates the cube with applied transmission curve over a known source to obtain AB magnitudes.

$$m_{AB}(t, z) = -2.5 \log \left[ \frac{\int_{-\infty}^{\infty} d\lambda \lambda \frac{L_\lambda [\lambda(1+z)^{-1}, (t(z))]}{(1+z)4\pi d_L^2(z)} R(\lambda)}{\int_{-\infty}^{\infty} d\lambda \lambda C_\lambda(\lambda) R(\lambda)} \right] \quad (2.7)$$

Here  $\lambda$  is the wavelength,  $z$  the redshift and  $R(\lambda)$  the filter transmission curve. We know that  $F = \frac{L_\lambda}{4\pi d^2}$ . Furthermore we can set  $z=0$ , as the cluster is inside of our galaxy. Finally, we want everything to be in terms of the wavelength and not the frequency. This means that we will have to convert  $C_\nu$  to  $C_\lambda$ . This can be done by using the following identity and  $\lambda\nu = c$ ,

$$\begin{aligned} \nu C_\nu &= \lambda C_\lambda \\ C_\lambda &= \frac{\nu}{\lambda} 3631 \text{ Jy} \\ &= \frac{c}{\lambda^2} 3631 \text{ Jy}. \end{aligned} \quad (2.8)$$

Plugging these into Eq. (2.7) we get

$$\begin{aligned} m_{AB} &= -2.5 \log \left[ \frac{\int_{-\infty}^{\infty} d\lambda \lambda F(\lambda) R(\lambda)}{\int_{-\infty}^{\infty} d\lambda \lambda C_\lambda(\lambda) R(\lambda)} \right] \\ &= -2.5 \log \left[ \frac{\int_{-\infty}^{\infty} d\lambda \lambda F(\lambda) R(\lambda)}{c \int_{-\infty}^{\infty} d\lambda \cdot 3631 \text{ Jy} \cdot \frac{1}{\lambda} R(\lambda)} \right]. \end{aligned} \quad (2.9)$$

If we then substitute the integrals for sums, we will be able to describe the discrete nature of our data cube in the following manner:

$$m_{AB} = -2.5 \log \left[ \frac{\sum \lambda \cdot F \cdot R}{c \cdot 3631 Jy \cdot \sum \frac{1}{\lambda} R} \right]. \quad (2.10)$$

Eq. (2.10) has subsequently been implemented into a Python script that can make white light images for a selected filter. These images are theoretically identical to HST images, apart from the fact that the Hubble images have a much smaller point spread function (PSF).

### Convoluting Hubble images

The difference in PSF between Hubble and MUSE images can cause light to fall in or out of the selected regions, and thus potentially contaminating the result. This can be corrected by convoluting the downloaded HST images with the MUSE PSF. If the two PSFs are similar in size, we would have to first deconvolve the HST PSF, but since the difference is so big we assume that the HST PSF is a delta function. We assume that the MUSE PSF can be described by a Gaussian. Next we choose a set of 10 stars in DS9 and make a region file in which the centroids of each star is saved. We then calculate the full width at half maximum (FWHM) of each star in several directions and take the standard deviation (std) corresponding to the average FWHM by using  $\sigma = FWHM/2.3548$ . If we then multiply the obtained std with the quotient between the MUSE and HST plate scales, we will obtain the size of the PSF in the HST images. These plate scales for MUSE and the HST are 0.2 and 0.04 arcsec/pix respectively, as seen in the headers of the respective images.

The convolution is achieved by using the convolution theorem, which states that the inverse Fourier transform of the product of two Fourier transformed quantities equals the convolution of these two. Or

$$a(\lambda) \otimes b(\lambda) = \mathcal{F}^{-1} (\mathcal{F}(a(\lambda)) \cdot \mathcal{F}(b(\lambda))). \quad (2.11)$$

With  $\otimes$  as the convolution symbol and  $a(\lambda)$  and  $b(\lambda)$  both a arbitrary function of wavelength.

Formally we would speak of a bi-dimensional, field spread function (FSF), described by a Moffat function and a spectral line spread function (LSF) (Bourguignon et al., 2011), but since we apply relatively complex filters to the cube, we chose to fit a Gaussian PSF profile to the three white light images, like described above.

## Magnitudes

To check this theory we compare the apparent AB magnitude for both images and see how close they are. This is done with help of the Aper Python package, which is translated from IDL (Landsman, 1993) by G.P.P.L. Otten MSc., implemented with a custom made python script that extracts photometric data from preselected DS9 regions. The flux is obtained from these white light images by taking the counts in the regions and subtracting the background

$$F = C_{star} - \frac{C_{sky}}{A_{sky}} \cdot A_{star}. \quad (2.12)$$

This is then converted into magnitudes as described in section 2.2.2. In future research these can give us certain parameters when fitting the photometry.

### 2.2.3 Integrated Spectra

Using a similar method as described in section 2.2.2, we can sum the MUSE data cube over the spatial directions to obtain a 1d spectrum for every concentric circle. These spectra can then be fed to a spectrum analysis package to see what parameters it will give back. An example of such software is STARLIGHT (Cid Fernandes et al., 2005).

Because of the fact that the spectra were taken from the ground, we get interference from the atmosphere. We applied a telluric correction, see Fig 2.7, provided by Dr. Kamann to the spectra and also masked out the sky lines at 5577, 6300 and 6363 nm. Besides that we cut the spectrum at 7151 onwards to remove the forest of emission lines in that wavelength range.

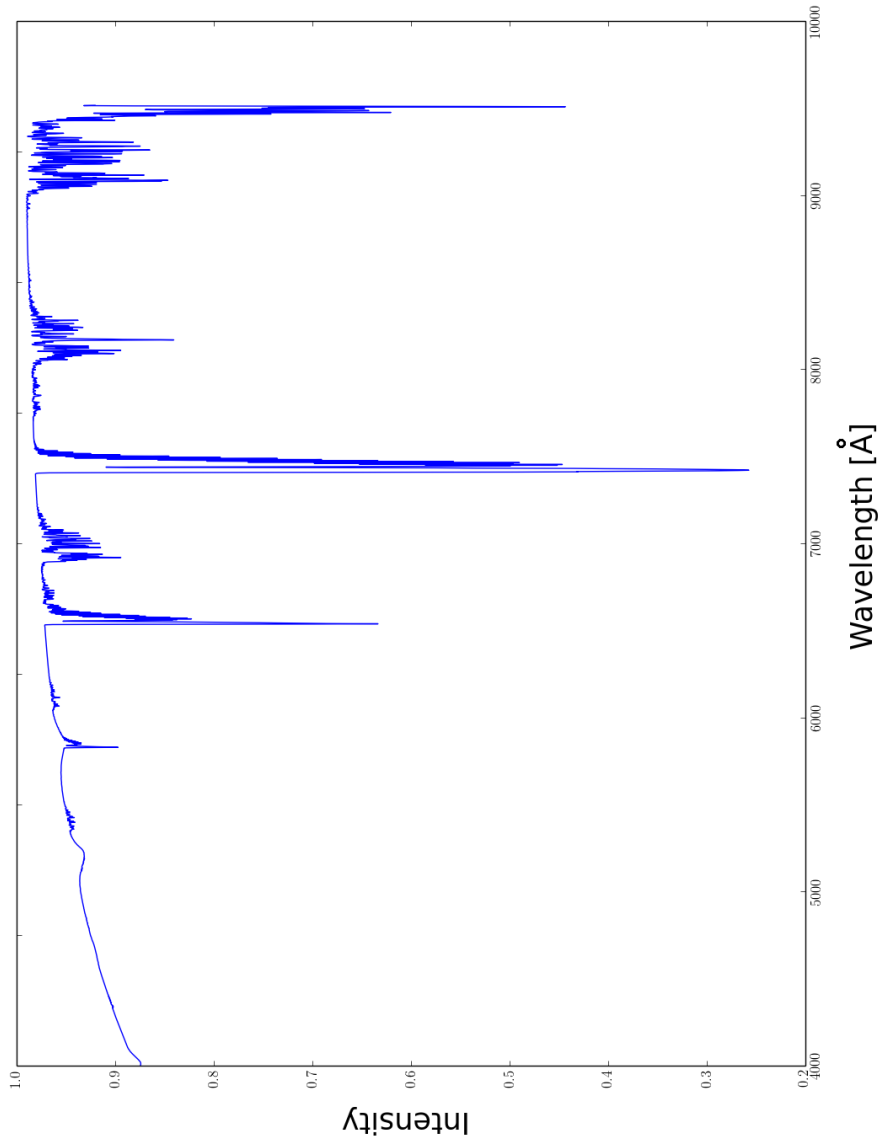


**Figure 2.7:** The telluric correction curve for the MUSE wavelength range. This curve would be multiplied with the MUSE spectra to remove certain atmospheric contaminations. The spectrum is made by dividing a model spectrum of a star by an observation of an astronomical photometric standard star.

## Starlight

The content of this section is again largely based on Conroy (2013) and Cid Fernandes et al. (2005). A summary of the two papers is given below.

It is possible to create composite stellar populations (CSPs) from SSPs by adding the star formation history (SFH), the chemical evolution of the population and interstellar dust, as can be seen in Figure 2.8. This is needed to describe features which would otherwise not be explainable by a single SSP. For the SFH we assume that the star formation rate (SFR) depends linearly on the gas density as often described by the  $\tau$ -model (Schmidt, 1959). The metallicity is often described even more simplistically by just a couple or even a single value for the entire CPS. The effects of these simplifications have not been studied thoroughly. Interstellar dust is harder to compensate as, as it blocks NIR and UV light but also emits IR radiation. These effects are usually modelled independently because of their geometrical effects. In our observations we lose light by either scattering or absorption. Light can be scattered in and out of the line of sight while absorption happens only along the line of sight. Attenuation is the total loss of light of a galaxy or GC due to dust, and can be corrected by comparing the spectra of the entire population with a model dustless spectrum of the same population. The emission of interstellar dust is non negligible at observed wavelengths and is caused by exposing the grains to interstellar radiation fields. Besides that the composition, size distribution and field strength all play a role in its behaviour. In this project we add an extinction correction of  $A_v = 0.56$  (Kamann et al., 2015) which is a normalisation factor for the reddening law used by the program. In our case this is the Cardelli, Clayton and Mathis law (Cardelli et al., 1989) with  $R_v = 3.1$ .

We fit our spectra with a CSP composed by the spectral synthesis code STARLIGHT. The observed input spectrum  $O_\lambda$  is fitted with a series of  $N_*$  SSP models. We model the line of sight stellar motions with a gaussian (G) centered at a velocity  $v_*$  with a dispersion  $\sigma_*$ . These assumptions together give us the model spectrum

$$M_\lambda = M_{\lambda 0} \left[ \sum_{j=1}^{N_*} x_j b_{j,\lambda} r_\lambda \right] \otimes G(v_*, \sigma_*). \quad (2.13)$$

This describes the fractional contribution to the model spectrum  $\lambda_0$  of every SSP model  $x_j$  ( $j = 1 \dots N_*$ ) with age  $t_j$  and metallicity  $Z_j$  and reddening  $r_j$ .

In this project we use a base of 15 SSPs with a metallicity of 0.004, which corresponds to ages ranging from  $10^6$  to  $1.434 \cdot 10^9$  years. These models are

chosen for their low metallicity to circumvent the -Age–Metallicity Degeneracy (Worthey, 1994) and force the program to fit old and low Z stars, rather than young, high Z stars. We will use either Chabrier or Salpeter IMF's, the Bruzual and Charlot (2003a) isochrome synthesis code along with the STELIB library.

The fit is then given by minimizing  $\chi^2$  in

$$\chi^2 = \sum_{\lambda} \left[ (O_{\lambda} - M_{\lambda}) w_{\lambda}^2 \right]^2. \quad (2.14)$$

Here  $w_{\lambda}$  is the weight factor that can be used to mask out bad pixels or sky residuals while also serving as the inverse error ( $w_{\lambda}^{-1}$ ) in the spectrum. This fit is run  $N_M = 6$  times using an Metropolis scheme, which slowly focuses on the most likely region without getting stuck in local minima. This returns the best possible fit of the spectrum, along with the awaited parameters.

### Error analysis

Because error propagation is impossible due to the use of the STARLIGHT package and because the steps are too complex, we get error estimates for our data by means of Monte Carlo resampling. We add the observational errors  $\sigma_{obs}$  from the MUSE data cube multiplied by a random number drawn from a normal distribution to our data before processing it. This noise is put in as  $\sigma_N = N(0, 1) \cdot \sigma_{obs}$  and is added to every pixel independently. After processing the data we then take the standard deviation for every one of the 28 regions to see the error on the value obtained from it. To get proper errors we need to make sure that we use enough Monte Carlo iterations. We are content with errors within a margin of 10%, which is equivalent to a S/N of 10. To find out how many iterations we need to achieve this S/N, we want to take the variance of the standard deviation as shown on the Wolfram Mathworld page (Wolfram Mathworld 2015).

$$\sigma_{\sigma_x} = \sigma_x \frac{\Gamma\left(\frac{n-1}{2}\right)}{\Gamma\left(\frac{n}{2}\right)} \sqrt{\frac{n-1}{2} - \left(\frac{\Gamma\left(\frac{n}{2}\right)}{\Gamma\left(\frac{n-1}{2}\right)}\right)^2}. \quad (2.15)$$

All that needs to be done is to bring the  $\sigma_x$  to the other side and solve numerically for 10, which shows that we need 51 iterations for a S/N of 10. Since it is always good to round this number up we take 100 iterations for our Monte Carlo resample. In Fig. 2.9 we can see a plot of S/N versus

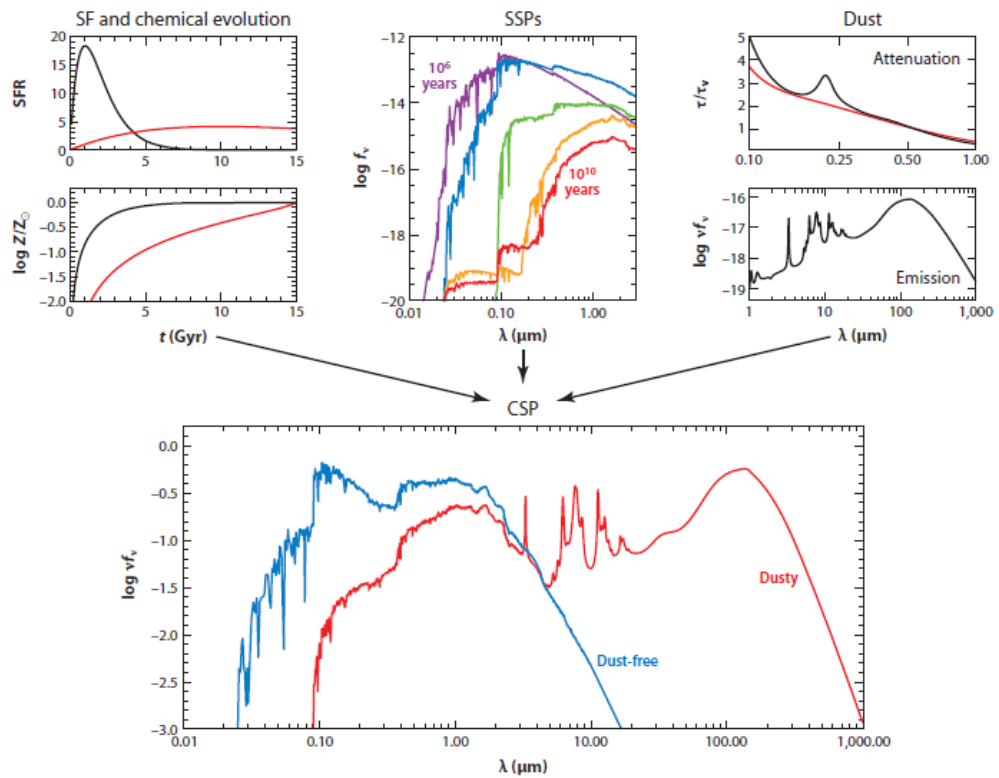


**Figure 2.8:** Overview of CPS composition. The upper panels show the three main ingredients for a CPS. The SFH and chemical composition, a set of SSPs and dust effects. Figure from (Conroy, 2013)

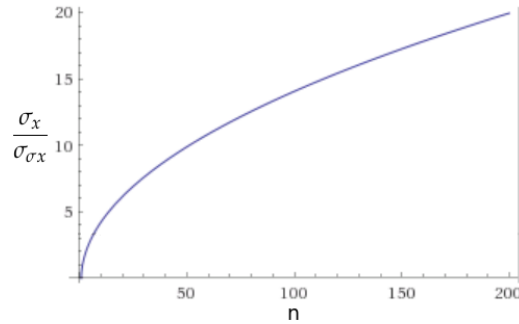


**Figure 2.9:** A plot of Eq. 2.15 showing the S/N obtained for a given amount of Monte Carlo iterations

the amount of iterations.

$$\frac{\sigma_x}{\sigma_{\sigma_x}} = \left( \frac{\Gamma\left(\frac{n-1}{2}\right)}{\Gamma\left(\frac{n}{2}\right)} \sqrt{\frac{n-1}{2} - \left(\frac{\Gamma\left(\frac{n}{2}\right)}{\Gamma\left(\frac{n-1}{2}\right)}\right)^2} \right)^{-1} = 10 \quad (2.16)$$

We will use these error estimates when looking at the difference between values obtained via STARLIGHT and values from Dr. Kamann.

We also wish to see if the results differ for the obtained parameters using different IMFs. This can be explored by subtracting a large amount of these Monte Carlo values for a given region and IMF from the same region and different IMF. By looking at the distribution of these differences we can see if there is an offset to the Gaussian. Because we care mostly for testing this method with large regions, we will only look at the largest circle.



## Results and Discussion

The results of both the photometric and spectral fitting with error estimates are summarized and compared to literature where possible.

### 3.1 Photometry

#### 3.1.1 Convolution

Because of the fact that we use the same regions in both HST and MUSE images, we have to keep in mind that the size of stars matters. Especially if the regions are arbitrary and can cut through stars. For this reason we wanted to have equally sized stars and thus convolved the HST images with their corresponding MUSE PSFs. For the F435W, F606W, F814W filters the obtained values for the standard deviation of the PSF are  $0.27''$ ,  $0.29''$  and  $0.23''$  respectively. In Fig. 3.1 we can see the result of such a convolution. Comparing the PSFs to the FWHM model for a given wavelength range without filters, on the 'MUSE Science Team Wiki', we see that these values match roughly within 15%.

#### 3.1.2 Comparing MUSE to Hubble

Comparing the AB magnitudes obtained via Eq. (2.10) we can see in Fig. 3.2 and Fig. 3.3 that while the values match roughly, there are still some noticeable discrepancies of up to 0.20 mag. The same problem is reported in Kamann et al. (2015) and no solution is given. For this reason we pay no further attention to the problem and accept that there is a residual uncertainty in the overall calibration. We can see that both the curves have

a large offset for the first few circles, that becomes smaller gradually and becomes stable at around at around  $10''$  in radius. The regions with a smaller radius are more sensitive to small mismatches between the Hubble and MUSE image. These mismatches become smaller as the regions become larger, which is what we would expect in such a situation. Possible causes could be mismatched coordinates, bleeding stars or errors in the convolution. We choose to disregard these points due to this reason and the reasons given at the end of section 2.2.1.

### 3.1.3 Integrated Spectra

For this section we use 5600 model spectra to compare to the spectrum of each of the 28 regions. Each region is sampled 100 times using the Monte Carlo method. This process is repeated twice for the two different IMFs. The extracted spectra were all corrected for tellurics and had the sky lines masked. Besides this we selected a region of the spectrum for normalisation in the range of  $6100 < \lambda < 6200$ , as can be seen in Fig. 3.4 and Fig. 3.5. Like described in section 3.1.3, we lock the extinction coefficient to  $A_v = 0.58$ , the maximal velocity dispersion to  $v_d = 80$  km/s. (With an initial value of  $v_0 = 50$  km/s.) The metallicity has been chosen to be 0.004. All other parameters are left free for fitting.

In Fig. 3.5 we can see that the obtained fit is quite poor. However, we can still use the spectra to derive total mass inside every region. These masses are compared to the masses provided by Dr. Kamann by dividing the two and plotting the result. In Fig. 3.6, we see that they match fairly well. For the largest region these values are  $640.7 \pm 170 M_\odot$  and  $463.79 \pm 170 M_\odot$  for Salpeter and Chabrier respectfully, compared to  $580.9 M_\odot$  obtained from dr. kammans data. We compared the values by dividing the derived masses by the provided mass. In this figure we have four sub-figures, two (a,c) showing the obtained mass for every individual Monte Carlo simulation for the Chabrier and Salpeter IMFs respectively. These calculations are used to estimate the errors on the remaining two figures (b,d). If we look at the errors in these images, then we see that the value for the error spikes up at certain radii. We think that this is because of the fact that the circles corresponding to these spikes cut trough one or more star. This means that any offset between the HST and MUSE images could push these stars in our out of the region, creating a measurable difference in flux. In the image we see that region 1, 8,11 and 22 cause increases in the error. Plotting these circles onto the cluster shows us that these circles do

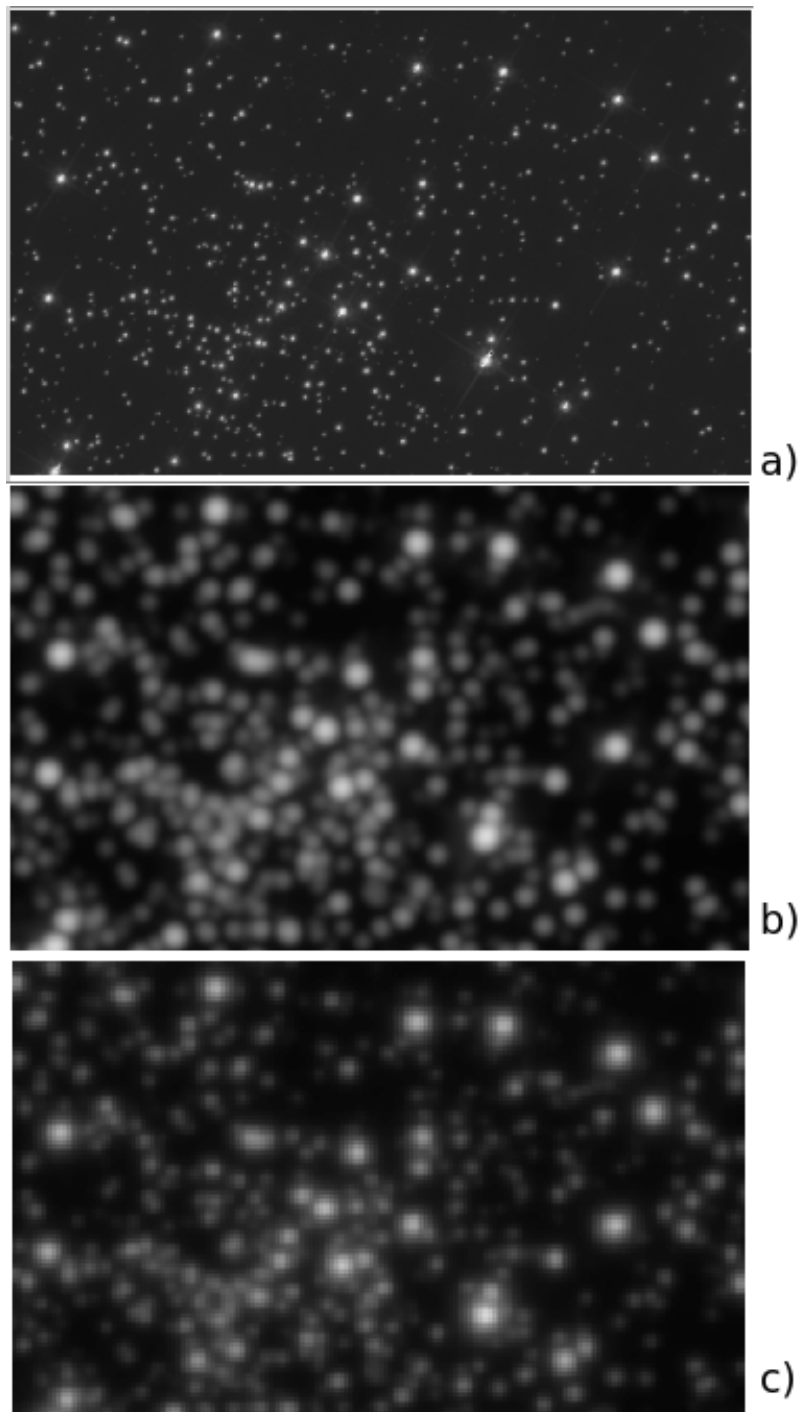


**Figure 3.1:** A triplet of images centered on RA 265.17314, Dec -53.673328 with a  $1 \times 0.5$  arcminute window. (a) The HST F606W image without convolution. (b) The same HST image with the applied MUSE PSF. (c) The MUSE image of the same region.

indeed cut through bright stars. Fig. 3.8 shows these circles with the others left out.

If we look with the naked eye, we can see that even though both IMFs match with the predicted mass within their errors, the Chabrier IMF seem to fit slightly better than the Salpeter IMF. For this reason we run some extra statistics to see if there is a slight bias towards one of the two IMFs. To achieve this we subtract the Chabrier and Salpeter derived masses for every region and use the 100 Monte Carlo values for the mass error estimate that were used above. With this we can fit a Gaussian to the data and look if it is offset from zero. The acquired values can be seen in Fig. 3.7a and hint toward a preference of the Salpeter IMF. Excluding the first 13 values, the offset of these points is 0.31, which is less than one standard deviation and therefore not statistically significant.

STARLIGHT also gave age estimates for every Monte Carlo run (Fig. 3.7b and Fig. 3.7c), allowing us to calculate the mean age per region and their errors. For the largest region, using the Charbrier and Salpeter IMF we get a  $\log(\text{age})$  of  $9.96 \pm 0.38$  and  $9.93 \pm 0.37$  respectively, which falls within the cluster age of  $10.13^{+0.01}_{-0.03}$  (Torres et al., 2015). The values have relatively low accuracy, probably because of the bad fit in Fig. 3.4. We chose for a logarithmic age because the distribution of ages did not resemble a Gaussian while the  $\log(\text{age})$  did, allowing us to get the Monte Carlo error estimates in the same way as the mass.

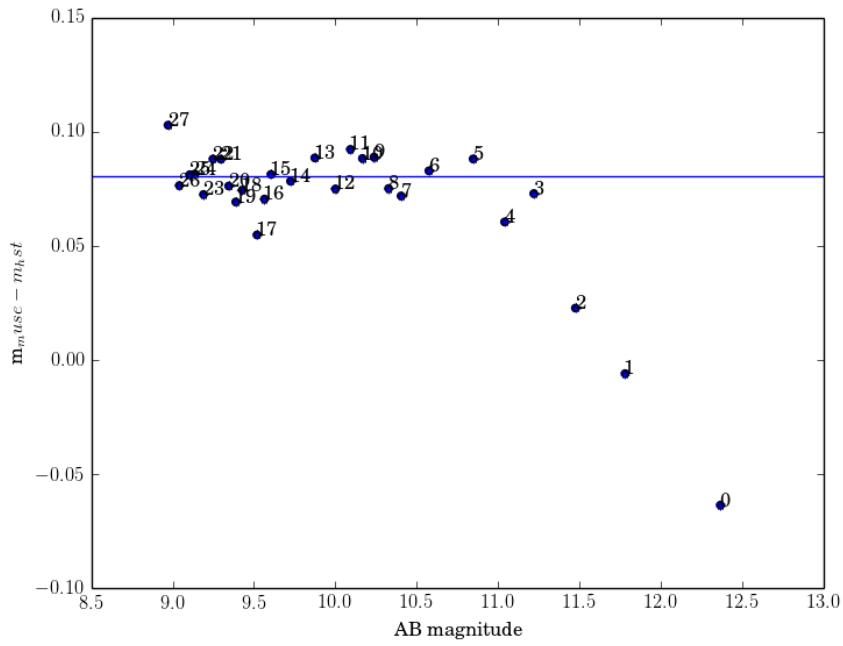


**Figure 3.2:** Magnitude difference for the F606W filter. Steady for big regions with a radius of about  $10''$  or more on a 0.8 mag offset.

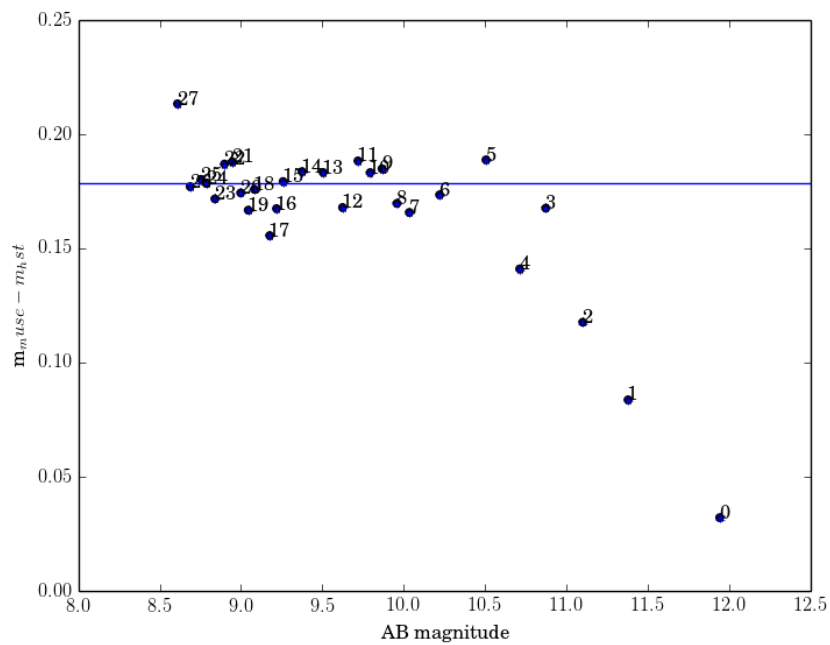


**Figure 3.3:** Magnitude difference for the F814W filter. Steady for big regions on a 0.17 mag offset.

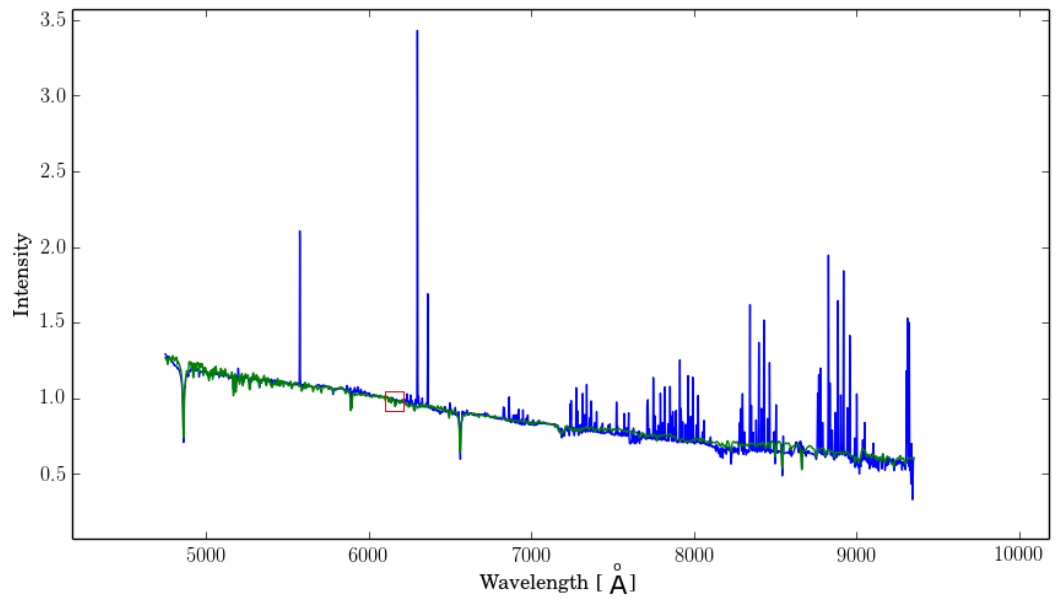


**Figure 3.4:** In blue the input spectrum obtained from the MUSE cube for the largest circle. In green the fit as given by STARLIGHT. In red the region used for normalisation. To avoid the sky the spectrum ( $\lambda > 7200 \text{ \AA}$ ) has been masked.

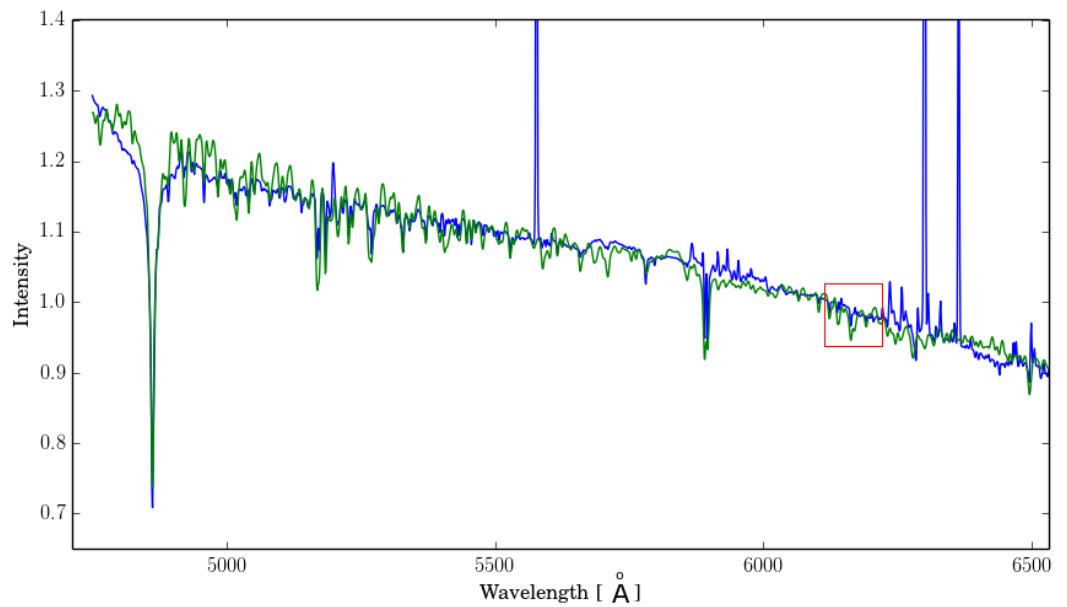


**Figure 3.5:** Zoomed in version of Fig. 3.4, showing the difference between the input and output spectra.

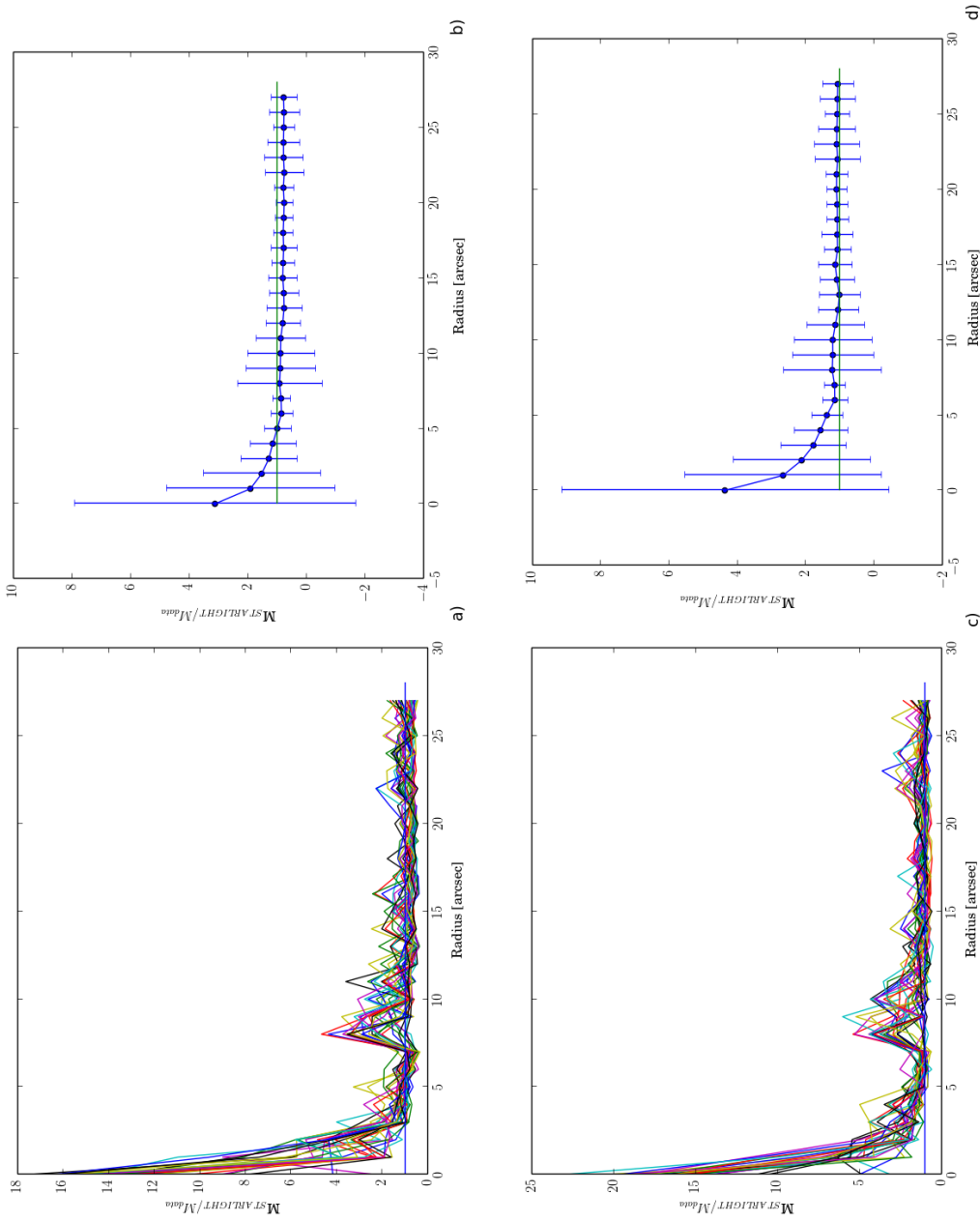


**Figure 3.6:** Masses derived by STARLIGHT divided by the mass provided by dr. Kamman (plotted as  $\frac{m_{STARLIGHT}}{m_{data}} = 1$ ) as a function of circle radius. (a) 100 Monte Carlo mass estimates with the Chabrier IMF for each of the regions, plotted to show the variation in estimate. (b) Derived mass for the regions while using the Chabrier IMF with errors estimated by Monte Carlo estimation. (c) 100 Monte Carlo mass estimates with the Salpeter IMF for each of the regions, plotted to show the variation in estimate. (d) Derived mass for the regions while using the Salpeter IMF with errors estimated by Monte Carlo estimation.

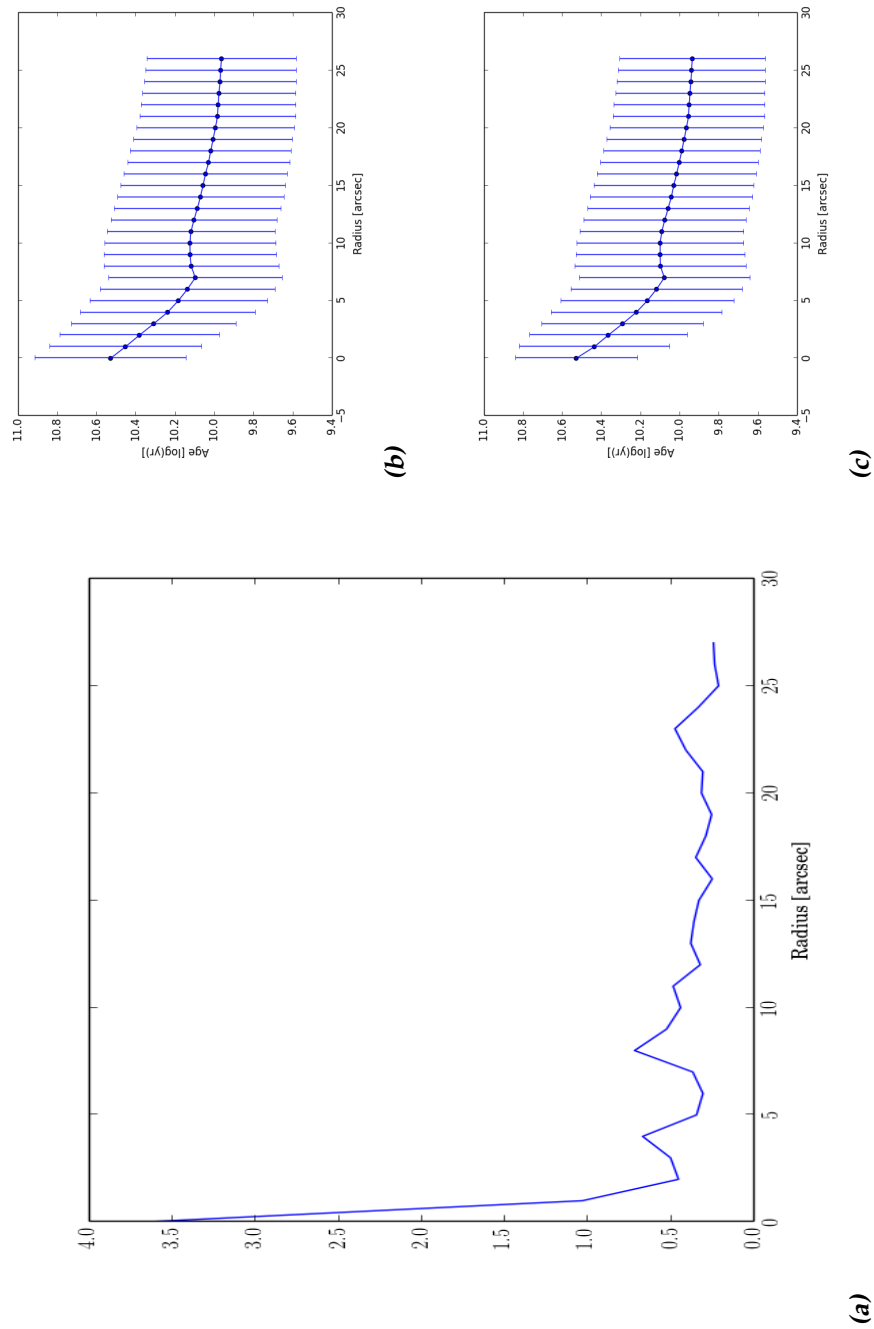


**Figure 3.7:** (a) The mean of the Gaussian of the difference between the Salpeter and Chabrier IMF as a function of radius. Excluding the first 13 points, it has an average value of 0.31, which is less than one standard deviation. (b,c) A plot showing the mean age for stars inside of each region using the Chabrier and Salpeter IMFs respectively.

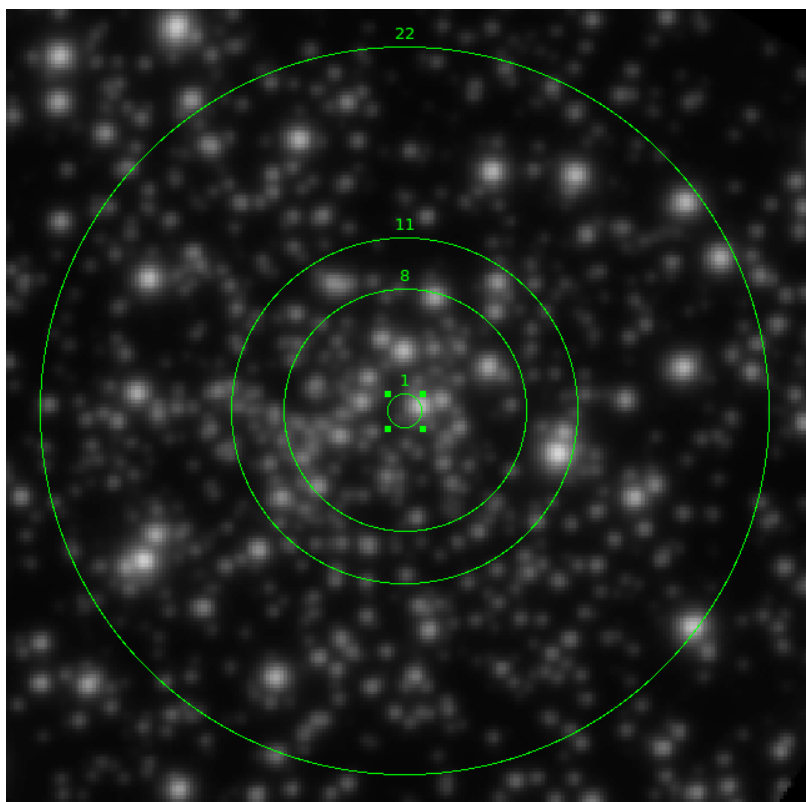


**Figure 3.8:** A plot of the cluster with the 1st, 8th, 11th and 22th ring shown.



## Conclusion

Using the MUSE instrument we were able to get both photometric and spectral data from globular cluster NGC 6397. From this data we were able to infer the age and mass of this cluster while setting a metallicity and IMF by creating integrated spectra over large areas of the cluster. The derived mass has some large fluctuations for radii smaller than 10 arcseconds. We think that this is because of the fact that mismatches between the HST and MUSE frames in either coordinates, quality of the estimated MUSE PSF that was used for convolution. However, for radii larger than 10" we find that most of these problems disappear and roughly the same result comes out for every consecutive region.

When comparing the obtained masses with literature values we found that the mass derived while using the Salpeter IMF fitted slightly better than the Chabrier IMF. Namely  $640.7 \pm 170 M_{\odot}$  and  $463.79 \pm 170 M_{\odot}$  for Salpeter and Chabrier respectfully, compared to  $580.9 M_{\odot}$ , obtained from summing dr. Kammans data over the largest area. After a statistical Monte Carlo test, we found that this difference is less than  $1\sigma$  and therefore not statistical. However, it would be interesting to repeat this process with a larger image, more regions and possibly other GCs. Increasing our sample space to allow for a conclusive answer.

The age also gave a result with large error bars, as can be seen in Fig. 3.7b and Fig. 3.7c. Using the age value for the largest region, we get a  $\log(\text{age})$  of  $9.96 \pm 0.38$  and  $9.93 \pm 0.37$  when using the Chabrier and Salpeter IMFs respectively. While the literature value of  $10.11^{+0.01}_{-0.03}$  falls within the error, the uncertainty is still rather large. These large errorbars are probably caused by the poor fits given by STARLIGHT, as can be seen in Fig. 3.5,

resulting in a large variation of age and mass, see Fig. 3.6. We also noted a large aberration near the 8th, 11th and 22rd circle that caused the errors to blow up. These are plotted in Fig 3.8 and show that all of these circles cut through a bright source. Similar to like mentioned above, any mismatches in coordinates could cause large aberrations if these stars could fall in or out of a circle between the two frames.

This made us conclude that while some quantities can be derived using this method, it should be studied further and that results obtained in this way should be regarded carefully. For a follow-up study on this method it would be interesting to add photometric results derived from the same regions. It could also be of interest to try differently shaped regions, perhaps the annuli of the used circles or rectangular regions, bearing a closer resemblance to long slit spectra. Furthermore more research should be done on larger areas, like the full cluster and compared to other GCs, mainly to get smaller errorbars.

## Acknowledgements

After spending a year on this research project I can honestly say that I have learned a lot about working with IFU data. I very much enjoyed the balance between theory and computational work and the chance to work with data from the recently commissioned MUSE instrument. Because of this I would like to express my gratitude to my supervisor, Professor Jarle Brinchmann, for his guidance and constructive critique. I would also like to thank Vivianni Cordeiro de Sousa Santos, Leindert Boogaard and Sebastiaan Haffert for their advice and suggestions concerning the project, as well as Sebastian Kamann and Tim-Oliver Husser from the Goettingen group for sharing their data with me. My grateful thanks are also extended to Dominique Petit dit de la Roche, Nikki Zabel, Bart Verhaar, Andrej Dvornik and Steph Cooper for proofreading my work to remove all the typos.

Finally I would like to thank my parents and Dominique for their continuing support and encouragement throughout my study.



# References

G. Alcaino, W. Liller, F. Alvarado, V. Kravtsov, A. Ipatov, N. Samus, and O. Smirnov. Multicolor NTT CCD photometry of the post-core-collapse globular cluster NGC 6397. *AJ*, 114:1067–1073, September 1997. doi: 10.1086/118537.

E. Aver, K. A. Olive, R. L. Porter, and E. D. Skillman. The primordial helium abundance from updated emissivities. 11:017, November 2013. doi: 10.1088/1475-7516/2013/11/017.

R. Bacon, S. Bauer, P. Boehm, D. Boudon, S. Brau-Nogu e, P. Caillier, L. Capoani, C. M. Carollo, N. Champavert, T. Contini, E. Daguis e, D. Dall e, B. Delabre, J. Devriendt, S. Dreizler, J. Dubois, M. Dupieux, J. P. Dupin, E. Emsellem, P. Ferruit, M. Franx, G. Gallou, J. Gerssen, B. Guiderdoni, T. Hahn, D. Hofmann, A. Jarno, A. Kelz, C. Koehler, W. Kollatschny, J. Kosmalski, F. Laurent, S. J. Lilly, J. Lizon, M. Lupias, S. Lynn, A. Manescau, R. M. McDermid, C. Monstein, H. Nicklas, L. Par es, L. Pasquini, A. P econtal-Rousset, E. P econtal, R. Pello, C. Petit, J.-P. Picat, E. Popow, A. Quirrenbach, R. Reiss, E. Renault, M. Roth, J. Schaye, G. Soucail, M. Steinmetz, S. Stroebele, R. Stuik, P. Weilbacher, H. Wozniak, and P. T. de Zeeuw. Probing unexplored territories with MUSE: a second generation instrument for the VLT. In *Society of Photo-Optical Instrumentation Engineers (SPIE) Conference Series*, volume 6269 of *Society of Photo-Optical Instrumentation Engineers (SPIE) Conference Series*, page 0, June 2006. doi: 10.1117/12.669772.

G. Bertelli, A. Bressan, C. Chiosi, F. Fagotto, and E. Nasi. Theoretical isochrones from models with new radiative opacities. *A&AS*, 106:275–302, August 1994.

S ebastien Bourguignon, Herv e Carfantan, Eric Slezak, and David Mary. Sparsity-based spatial-spectral restoration of muse astrophysical hyper-

- spectral data cubes. In *Hyperspectral Image and Signal Processing: Evolution in Remote Sensing (WHISPERS), 2011 3rd Workshop on*, pages 1–4. IEEE, 2011.
- G. Bruzual and S. Charlot. Stellar population synthesis at the resolution of 2003. *MNRAS*, 344:1000–1028, October 2003a. doi: 10.1046/j.1365-8711.2003.06897.x.
- G. Bruzual and S. Charlot. GALAXEV:, 2003b.
- G. Bruzual and S Charlot. GALAXEV (Version 2003). August 2003c.
- J. A. Cardelli, G. C. Clayton, and J. S. Mathis. The relationship between infrared, optical, and ultraviolet extinction. *ApJ*, 345:245–256, October 1989. doi: 10.1086/167900.
- G. Chabrier. Galactic Stellar and Substellar Initial Mass Function. *PASP*, 115:763–795, July 2003. doi: 10.1086/376392.
- S. Charlot and A. G. Bruzual. Stellar population synthesis revisited. *ApJ*, 367:126–140, January 1991. doi: 10.1086/169608.
- R. Cid Fernandes, A. Mateus, L. Sodré, G. Stasińska, and J. M. Gomes. Semi-empirical analysis of Sloan Digital Sky Survey galaxies - I. Spectral synthesis method. *MNRAS*, 358:363–378, April 2005. doi: 10.1111/j.1365-2966.2005.08752.x.
- C. Conroy. Modeling the Panchromatic Spectral Energy Distributions of Galaxies. *ARA&A*, 51:393–455, August 2013. doi: 10.1146/annurev-astro-082812-141017.
- D. A. Forbes and T. Bridges. Accreted versus in situ Milky Way globular clusters. *MNRAS*, 404:1203–1214, May 2010. doi: 10.1111/j.1365-2966.2010.16373.x.
- M. Fukugita, T. Ichikawa, J. E. Gunn, M. Doi, K. Shimasaku, and D. P. Schneider. The Sloan Digital Sky Survey Photometric System. *AJ*, 111:1748, April 1996. doi: 10.1086/117915.
- L. Girardi, A. Bressan, G. Bertelli, and C. Chiosi. Evolutionary tracks and isochrones for low- and intermediate-mass stars: From 0.15 to 7  $M_{\text{sun}}$ , and from  $Z=0.0004$  to 0.03. *A&AS*, 141:371–383, February 2000. doi: 10.1051/aas:2000126.
- W. E. Harris. VizieR Online Data Catalog: Globular Clusters in the Milky Way (Harris, 1996). *VizieR Online Data Catalog*, 7195:0, November 1996.
- J. S. Heyl, H. Richer, J. Anderson, G. Fahlman, A. Dotter, J. Hurley, J. Kalirai, R. M. Rich, M. Shara, P. Stetson, K. A. Woodley, and D. Zurek. Deep

- Hubble Space Telescope Imaging in NGC 6397: Stellar Dynamics. *ApJ*, 761:51, December 2012. doi: 10.1088/0004-637X/761/1/51.
- T.-O. Husser, S. Kamann, and S. Dreizler. The MUSE view on NGC 6397 -I. Methods and first results. 2015.
- S Kamann, H-O. Husser, Dreizler, and the MUSE consortium. MUSE crowded field 3D spectroscopy of 10000 stars in the globular cluster NGC 6397. *Å*, June 2015.
- P. Kroupa. On the variation of the initial mass function. *MNRAS*, 322: 231–246, April 2001. doi: 10.1046/j.1365-8711.2001.04022.x.
- W. B Landsman. On the variation of the initial mass function. *Astronomical Data Analysis Software and Systems II, A.S.P. Conference Series*, 52:246, 1993.
- J.-F. Le Borgne, G. Bruzual, R. Pelló, A. Lançon, B. Rocca-Volmerange, B. Sanahuja, D. Schaerer, C. Soubiran, and R. Vílchez-Gómez. STELIB: A library of stellar spectra at  $R \sim 2000$ . *A&A*, 402:433–442, May 2003. doi: 10.1051/0004-6361:20030243.
- J. Mack, R. L. Gilliland, J. Anderson, and M. Sirianni. WFC Zeropoints at -80C. Technical report, May 2007.
- E. Martinazzi, A. Pieres, S. O. Kepler, J. E. S. Costa, C. Bonatto, and E. Bica. Probing mass segregation in the globular cluster NGC 6397. *MNRAS*, 442:3105–3111, August 2014. doi: 10.1093/mnras/stu1032.
- G. E. Miller and J. M. Scalo. The initial mass function and stellar birthrate in the solar neighborhood. *ApJS*, 41:513–547, November 1979. doi: 10.1086/190629.
- J. B. Oke and J. E. Gunn. Secondary standard stars for absolute spectrophotometry. *ApJ*, 266:713–717, March 1983. doi: 10.1086/160817.
- C. H. Payne. *Stellar Atmospheres; a Contribution to the Observational Study of High Temperature in the Reversing Layers of Stars*. PhD thesis, RADCLIFFE COLLEGE., 1925.
- T. H. Puzia, R. P. Saglia, M. Kissler-Patig, C. Maraston, L. Greggio, A. Renzini, and S. Ortolani. Integrated spectroscopy of bulge globular clusters and fields. I. The data base and comparison of individual Lick indices in clusters and bulge. *A&A*, 395:45–67, November 2002. doi: 10.1051/0004-6361:20021283.
- E. E. Salpeter. The Luminosity Function and Stellar Evolution. *ApJ*, 121: 161, January 1955. doi: 10.1086/145971.

- R. P. Schiavon, J. A. Rose, S. Courteau, and L. A. MacArthur. A Library of Integrated Spectra of Galactic Globular Clusters. *ApJS*, 160:163–175, September 2005. doi: 10.1086/431148.
- M. Schmidt. The Rate of Star Formation. *ApJ*, 129:243, March 1959. doi: 10.1086/146614.
- M. Shara. The Deepest Far-UV Imaging Survey of Globular Clusters: NGC 6752 and NGC 6397. HST Proposal, July 2000.
- S. Torres, E. García-Berro, L. G. Althaus, and M. E. Camisassa. The white dwarf population of NGC 6397. *A&A*, 581:A90, September 2015. doi: 10.1051/0004-6361/201526157.
- P. M. Weilbacher, O. Streicher, T. Urrutia, A. Pécontal-Rousset, A. Jarno, and R. Bacon. The MUSE Data Reduction Pipeline: Status after Preliminary Acceptance Europe. In N. Manset and P. Forshay, editors, *Astronomical Data Analysis Software and Systems XXIII*, volume 485 of *Astronomical Society of the Pacific Conference Series*, page 451, May 2014.
- P. Westera, M. Samland, G. Bruzual, and R. Buser. The BaSeL 3.1 models: metallicity calibration and application. In T. Lejeune and J. Fernandes, editors, *Observed HR Diagrams and Stellar Evolution*, volume 274 of *Astronomical Society of the Pacific Conference Series*, page 166, 2002.
- Wolfram Mathworld 2015. Standard deviation distribution. URL [mathworld.wolfram.com/StandardDeviationDistribution.html](http://mathworld.wolfram.com/StandardDeviationDistribution.html).
- G. Worthey. Comprehensive stellar population models and the disentanglement of age and metallicity effects. *ApJS*, 95:107–149, November 1994. doi: 10.1086/192096.